

A Scalable Synthesis Pathway to Nanoporous Metal Structures

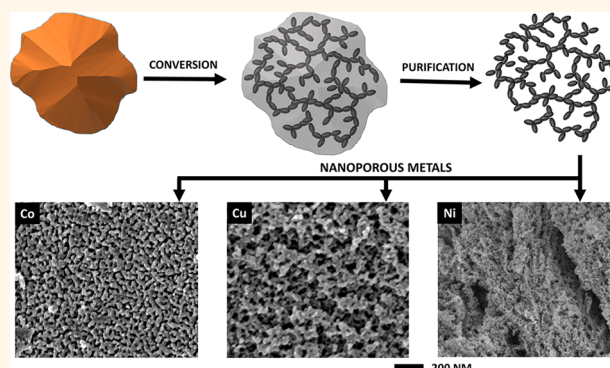
Christopher Coaty, Hongyao Zhou, Haodong Liu, and Ping Liu*[✉]

Department of NanoEngineering, University of California, San Diego, La Jolla, California 92093, United States

S Supporting Information

ABSTRACT: A variety of nanoporous transition metals, Fe, Co, Au, Cu, and others, have been readily formed by a scalable, room-temperature synthesis process. Metal halide compounds are reacted with organolithium reductants in a nonpolar solvent to form metal/lithium halide nanocomposites. The lithium halide is then dissolved out of the nanocomposite with a common organic solvent, leaving behind a continuous, three-dimensional network of metal filaments that form a nanoporous structure. This approach is applicable to both noble metals (Cu, Au, Ag) and less-noble transition metals (Co, Fe, Ni). The microstructures of these nanoporous transition metals are tunable, as controlling the formation of the metal structure in the nanocomposite dictates the final metal structure. Microscopy studies and nitrogen adsorption analysis show these materials form pores ranging from 2 to 50 nm with specific surface areas from 1.0 m²/g to 160 m²/g. Our analysis also shows that pore size, pore volume, and filament size of the nanoporous metal networks depend on the mobility of target metal and the amount of lithium halide produced by the conversion reaction. Further, it has been demonstrated that hybrid nanoporous structures of two or more metals could be synthesized by performing the same process on mixtures of precursor compounds. Metals (e.g., Co and Cu) have been found to stabilize each other in nanoporous forms, resulting in smaller pore sizes and higher surface areas than each element in their pure forms. This scalable and versatile synthesis pathway greatly expands our access to additional compositions and microstructures of nanoporous metals.

KEYWORDS: nanoporous metals, nanopores, nanocomposites, lithium conversion reactions, transition metals, three-dimensional nanostructures



Nanoporous metals (NPMs) are nanostructured pure metals with pores ranging from approximately 1 to 100 nm in diameter. They have been sought-after for their combination of metallic characteristics and nanostructured size-effect properties. They retain the desirable features of bulk metal, such as thermal/electrical conductivity, ductility, and malleability, while gaining beneficial nanostructured properties, such as low density and high surface area.¹ It has also been reported that these nanostructured metals exhibit size-enhanced effects, such as higher catalytic activity and plasmonic resonance.^{2–4} Their high surface area also marks them as promising materials for battery and capacitor electrodes.^{5,6} Further, NPMs are being explored for actuation applications because the topology and connectivity of these ligamented networks can be modulated with surface charge, causing dimensional change.⁷

Many synthesis routes for NPMs have been developed in the past 30 years,^{8,9} the oldest and most widely researched being the dealloying method. This method involves chemically or electrochemically removing the less-noble element from an

alloy, leaving behind a NPM.^{10,11} The prototypical example of this technique is the synthesis of nanoporous gold by etching the silver from a silver-gold alloy. Dealloying can produce structures with tunable porosities by varying reaction conditions and alloy compositions and is most effective when the target is a more noble metal (Au, Ag, Cu, Pt, Pd).^{1,11,12} The formation of NPMs *via* dealloying has been explained by a continuum model by Erlebacher *et al.* which states that pores form when the less-noble alloy component dissolves and the noble element atoms left behind are continuously driven to aggregate into two-dimensional clusters by phase separation at the solid–electrolyte interface.¹² It is also possible to use dealloying to fabricate NPMs of less-noble transition metals (e.g., Ni, Fe, Co, *etc.*) from their respective alloys with even more reactive metals such as Al.¹³ In addition, there are more specialized synthesis methods for less-noble NPMs, such as

Received: September 19, 2017

Accepted: January 8, 2018

Published: January 8, 2018

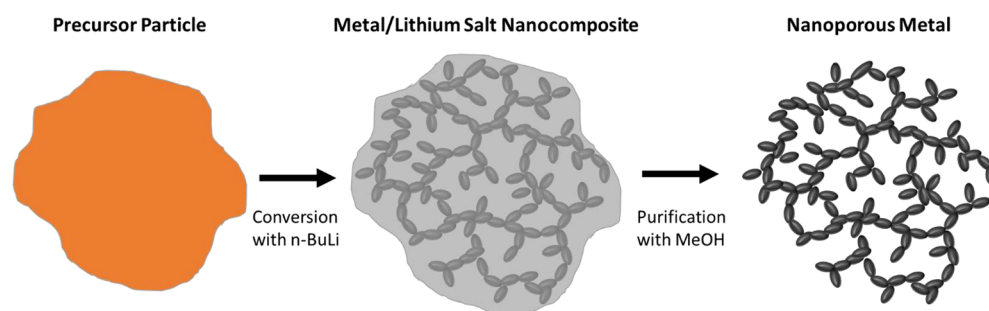


Figure 1. Illustration of NPM preparation *via* conversion reaction synthesis. An anhydrous transition-metal halide precursor (typically a chloride compound in this study) is reacted with *n*-BuLi and converted to a metal/lithium halide nanocomposite. The lithium halide is removed by dissolving it with methanol, leaving behind a NPM.

combustion synthesis,⁹ block copolymer templating,¹⁴ or directed assembly of metal nanoparticles.^{15,16}

This study details a simple, versatile, scalable synthesis route to NPMs *via* solid-state conversion reactions. Unlike the dealloying process, where the porous structure forms simultaneously while removing the less-noble element of an atomically mixed alloy, this method first fashions a nanocomposite of the desired pure metal with an ionic compound that can be removed by dissolution with a common organic solvent. This method is qualitatively similar to dealloying and other selective etching processes employed in nanomaterials synthesis, such as the techniques used to make MXenes.^{17,18} The advantage of this process is that it utilizes an organic solvent rather than an acid as an etchant, so it is applicable to both noble and less-noble pure metals, as well as metal mixtures and alloys. Access to these nanoporous transition-metal systems is particularly relevant to application in catalysis and magnetic materials, where alloys and nanometer-scale mixtures are highly desired.^{9,19,20}

Conversion reactions between lithium and transition-metal halides have been previously studied to yield high capacity battery electrodes. These reactions follow the general formula, $MA_x + xLi \rightarrow M + xLiA$, where the transition-metal halide (MA_x) is reduced by Li to form a pure metal (M) and a corresponding lithium halide (LiA).²¹ For example, the reaction between Li and FeF_3 has been studied extensively due to its theoretical energy density of 1750 Wh/kg, 2–3 times the capacity of state-of-the-art oxide materials.^{22,23} A TEM study observed that after discharge and complete conversion of an FeF_3 battery cathode following the equation above, the morphology of the Fe/LiF composite consisted of an “interconnected” and “bicontinuous” network of Fe nanoparticles surrounded by a LiF matrix.²⁴ The study observed that the Fe nanoparticles were approximately 2–3 nm in width. We reasoned that if the LiF was removed from the nanocomposite without damaging the Fe nanoparticle network, the resulting material would be a NPM.

RESULTS AND DISCUSSION

Nanoporous Pure Metals (NPMs). To employ the conversion reaction for the synthesis of NPMs, a chemical method is more desirable than an electrochemical one in terms of scalability and material purity. We chose to conduct the reactions at ambient temperatures using a reducing agent in a solution. The selection rule is that both the transition-metal halide and the lithium halide should be insoluble in the solution containing the reducing agent. Then, the lithium halide must be soluble in a separate solution which is stable toward the metal.

We chose an organolithium reducing agent, specifically *n*-butyllithium in hexane, which met all requirements.²⁵ Since LiF is difficult to dissolve with common solvents, we focused on chloride and bromide compounds because the LiCl or LiBr produced by the reaction is easily dissolved with a variety of common organic solvents such as ethanol, acetone, and methanol. We chose methanol in this study because most lithium halides and transition-metal halides have higher solubility in methanol compared to other organic solvents. This concept for conversion synthesis of NPMs is illustrated in Figure 1.

We utilized this conversion synthesis method to prepare nanoporous Co, Fe, Ni, Cu, Ag, and Au from their respective chloride precursors. Scanning electron microscope (SEM) images of the resulting NPMs are displayed in Figure 2a–h.

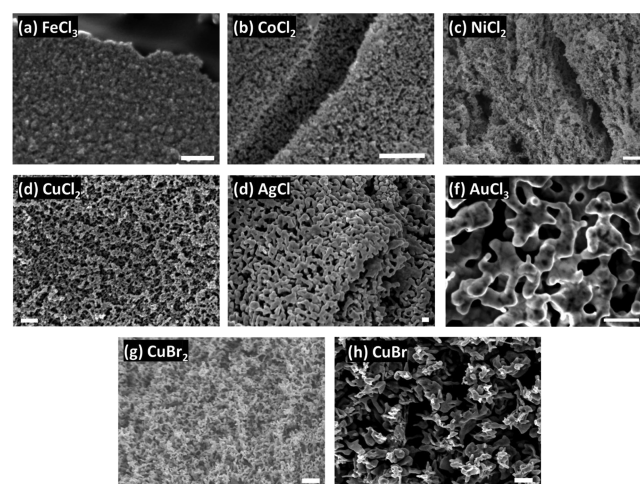


Figure 2. SEM images of nanoporous pure metals from chloride and bromide precursors. The precursor name is displayed over the SEM image of its corresponding pure NPM product after *n*-BuLi conversion and methanol purification. All images have 200 nm scale bars. (a) Fe from $FeCl_3$, (b) Co from $CoCl_2$, (c) Ni from $NiCl_2$, (d) Cu from $CuCl_2$, (e) Ag from $AgCl$, (f) Au from $AuCl_3$, (g) Cu from $CuBr_2$, (h) Cu from $CuBr$.

Qualitatively, each porous structure is a network of thin metal filaments with each precursor producing a different morphology with a characteristic filament thickness and network density. Nanoporous Fe from the $FeCl_3$ precursor showed exceptionally small pore size, and its features are difficult to discern from SEM alone, so the sample was also characterized with transmission electron microscopy (TEM), shown in Figure 3.

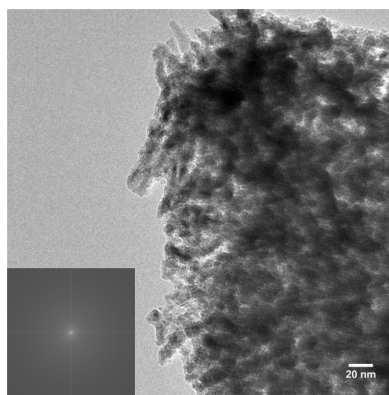


Figure 3. TEM images of nanoporous Fe synthesized from FeCl_3 precursor with the inset showing the electron diffraction pattern.

The TEM images show that the nanoporous Fe is made of similar randomly packed filaments to the other samples, but at a smaller length scale of a few nanometers. The electron diffraction pattern indicates that the nanoporous Fe is apparently amorphous.

Both the nanocomposites and the purified NPMs were characterized *via* X-ray diffraction (XRD) to confirm the complete conversion of each precursor to a metal/Li halide nanocomposite and complete removal of the Li halide after the methanol purification. Fourier-transform infrared spectroscopy (FTIR) and energy dispersive X-ray spectroscopy (EDX) also confirm that no residual organic compounds remain in the nanocomposites after the conversion reaction, as shown in [Supporting Information](#) (Figures S7 and S8). XRD characterization of the composites shows distinct peaks for both the Li halide and the target metal, indicating that they exist in the nanocomposite as two distinct phases ([Figure 4](#) and [Figure S1](#)). All samples show a degree of crystallographic peak broadening; a sign of nanocrystal formation. For Co and Fe samples, the peak broadening is so extreme that the peaks are barely perceptible, suggesting that the metal crystal structure for these samples is largely amorphous.^{26,27}

We employed Brunauer–Emmett–Teller (BET) analysis on the purified NPMs to measure specific surface area and to estimate pore size distribution and cumulative pore volume. N_2 adsorption–desorption isotherms and pore size distributions are displayed in [Figure 5](#) and [Figure S2](#), while structural and surface data for all samples are tabulated in [Table 1](#) for comparative analysis. When comparing the porous structures,

average pore width and ligament thickness correlate with one another and are both inversely proportional to specific surface area. All samples produce type IV N_2 adsorption–desorption isotherms,²⁸ and for samples with exceptionally small pore width, their isotherms exhibit type H3 hysteresis between the adsorption and desorption curves.²⁹ This phenomenon is indicative of capillary condensation of the nitrogen and has been previously documented in similar porous metal and metal oxide structures.^{30–32} The adsorption–desorption isotherm hysteresis only appears for samples with pore width <10 nm and increases as pore width shrinks, as shown in [Figure 5](#).

The thermodynamic driving force behind the reaction is the difference in electrochemical potential between the precursors and the reducing agent. Using *n*-butyllithium as the reducing agent requires the precursor's electrochemical potential to be higher than -2.05 V *vs* SHE.³³ The reaction then proceeds spontaneously and forms structures similar to those described by conversion reaction battery electrode studies.³⁴ The conversion initiates on the surface of the precursor particles. We hypothesize that the volume expansion associated with the reaction (ranging from 5% to 30%, shown in [Table S1](#)) causes fractures on the surface of the nanocomposites, opening further pathways for the *n*-BuLi solution to permeate into the sample and continue the reaction until the precursor is depleted. The dense metal coalesces into a ligamented network which is surrounded by the more abundant lithium halide. Further study is planned to develop a detailed understanding of the formation mechanism, but the following discussion on observed data trends offers initial insights.

The specific dimensions of the metal network are affected by both the target metal and its respective precursor. This is the cause of the large discrepancy in the specific surface area of the NPMs in [Table 1](#), which varies from 1 to over 160 m^2/g . Each metal ligament in the nanocomposite is the collection of the metal atoms that were locally available in the precursor. Therefore, we postulate that precursor composition and metal atomic mobility play a role in determining the network morphology during the conversion reaction. Metals with higher atomic mobility migrate and agglomerate over a longer distance, which allows more atoms to gather and coalesce into thicker ligaments with greater separation. When comparing the trends in specific surface area and pore size of the different NPMs, they approximately correlate to trends in the metals' diffusion coefficients.

Previous studies and models show Cu, Ag, and Au are generally more mobile and have high diffusion coefficients,

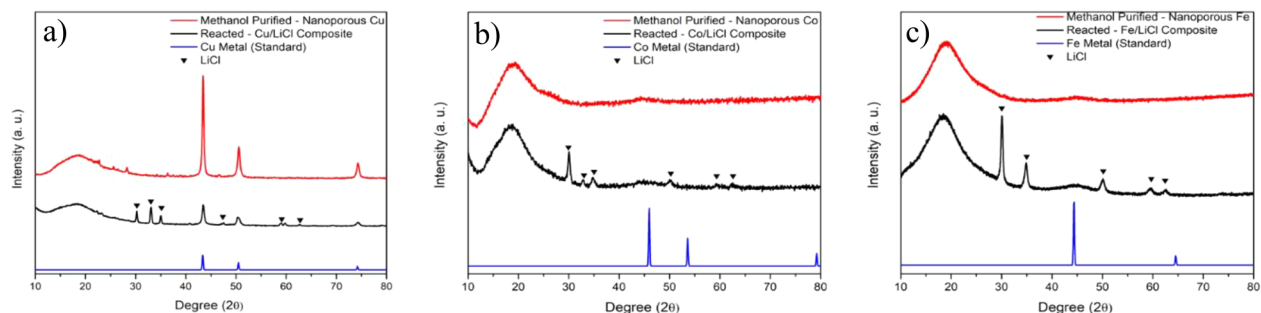


Figure 4. XRD patterns of three metal/LiCl nanocomposites and their corresponding NPMs after methanol purification. Also included are standard diffraction patterns for each metal from the Inorganic Crystal Structure Database (ICSD).⁴⁵ Peaks assigned to LiCl are denoted. (a) Nanoporous Cu from CuCl_2 ; (b) nanoporous Co from CoCl_2 ; and (c) nanoporous Fe from FeCl_3 . XRD data for additional samples are shown in [Figure S1](#).

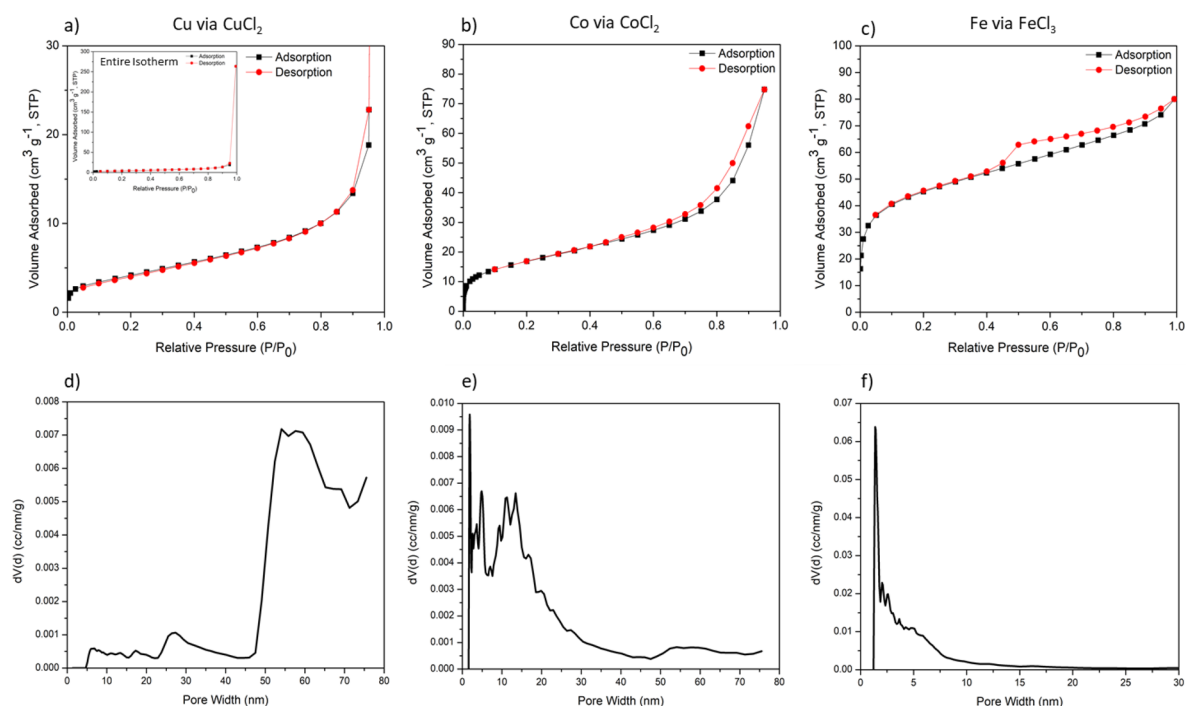


Figure 5. BET N_2 adsorption–desorption isotherms (a–c) and pore size distributions (d–f) for three NPMs synthesized from chloride precursors. Data from additional samples are provided in Figure S2. (a and d) Nanoporous Cu; (b and e) nanoporous Co; and (c and f) nanoporous Fe.

Table 1. Physicochemical Properties of Nanoporous Metals and Mixed Nanoporous Metals

Nanoporous Metal (NPM)	Conversion Reaction Data		Surface Analysis				Structure Analysis		
	Precursor	Specific volume % lithium halide in composite	Specific surface area (m^2/g)	Ave pore width (nm)	Cumulative pore volume (cm^3/g)	Theoretical cumulative pore volume (cm^3/g)	Approx. ligament thickness (nm)	Crystallite size (nm)	Metal crystal structure
Fe	$FeCl_3$	89.65	161.95	1.8	0.124	1.1	8	--	Amorphous
	$FeCl_2$	85.23	131.39	3.5	0.115	0.734	10	--	Amorphous
Co	$CoCl_2$	86.09	87.18	7.1	0.172	0.695	15	--	Amorphous
Ni	$NiCl_2$	86.14	70.92	19	0.395	0.698	20	5	FCC(ccp)-Cu
Cu	$CuCl_2$	85.24	15.03	40	0.408	0.644	40	20	FCC(ccp)-Cu
	$CuBr_2$	87.5	14.77	41	0.416	0.787	40	20	FCC(ccp)-Cu
	$CuBr$	77.9	1.06	56	0.011	0.393	200	35	FCC(ccp)-Cu
Ag	$AgCl$	66.57	9.69	26	0.0621	0.19	50	35	FCC(ccp)-Cu
Au	$AuCl_3$	85.66	5.343	41	0.054	0.312	90	30	FCC(ccp)-Cu
Mixed Nanoporous Metals (MNPM)	Coprecipitated Precursors	Mixed Metal Weight Ratio							
AuCu	$AuCl_3 + CuCl_2$	1:1	24.37	55	0.287	-	15	24 (Au)	FCC(ccp)-Cu
		3:2	14.64	36	0.131	-	15	24 (Au)	FCC(ccp)-Cu
CuCo	$CuCl_2 + CoCl_2$	1:1	115.7	2.0	0.281	-	30	5.7 (Cu)	FCC(ccp)-Cu
FeCo	$FeCl_2 + CoCl_2$	1:1	101.9	5.1	0.118	-	16 (Co) 10 (Fe)	-	Amorphous

resulting in larger ligaments and pores than Ni, Co, and Fe, which generally have lower diffusion coefficients, with Fe often having the smallest diffusion coefficient of the metals in this

study.^{35–37} A review on the diffusion, solubility, and electrical activity of transition metals in silicon by Weber³⁷ supports this trend, showing that diffusion coefficient for 3d transition metals

decreases with atomic number, ranging from 10^{-4} cm²/s for Cu to 10^{-6} cm²/s for Fe. Further, individual precursors for the same target NPM produce distinct porous structures. When comparing FeCl₂ and FeCl₃, FeCl₂ produces nanoporous Fe with lower specific surface area, larger pore width, and a smaller N₂ adsorption isotherm hysteresis. Similarly, products from CuCl₂ and CuBr₂ conversions are nearly identical, while the product of the CuBr conversion shows a drastically lower specific surface area and thicker ligaments, a phenomenon visible in the SEM images in Figure 2g-h. This suggests that the lithium halide physically hinders the agglomeration of the metal atoms over larger length scales during the reaction, encouraging the formation of finer ligament networks. For nanoporous Fe from the FeCl₃ precursor, a combination of a low-mobility element and a high lithium halide production when reacted with *n*-BuLi (3 mol of LiCl produced per mole FeCl₃) results in the highest surface area and smallest pore size of any sample in this study.

The purification phase of this synthesis method is similar to the dealloying processes in that it involves the selective dissolution of one component of a binary mixture. The fundamental difference is that dealloying involves a metal alloy of two highly miscible phases that form a solid solution (such as an Au-Ag alloy for nanoporous gold),^{1,12} while conversion synthesis involves a mixture of two immiscible phases. Originally, we hypothesized that the interconnected metal networks would be formed in the metal/lithium halide nanocomposites and would remain unaltered by removing the lithium halide. However, BET and XRD data contradict this assertion and show evidence of reconstruction during purification. For all samples, we compared the cumulative pore volume calculated by BET with the specific volume of the lithium halide present in the nanocomposites. As Table 1 shows, every sample measures much lower cumulative pore volume than predicted. This discrepancy is a convincing indicator that the metal ligament networks alter when the halide is removed with methanol.

For samples that exhibited well-defined XRD peaks (Cu, Ag, Au, Ni), this change is apparent in the diffraction patterns as the peaks corresponding to metals sharpen noticeably after methanol purification (Figure 1 and Figure S1). Table 2 shows

Table 2. Metal Nanocrystal Sizes Calculated from XRD Peak Broadening via the Scherrer Formula³³

Metal	Precursor(s)	Metal Nanocrystal Size in Nanocomposite (nm)	Metal Nanocrystal Size in Porous Structure After Purification (nm)
Cu	CuCl ₂	18	22
	CuBr ₂	16	21
	CuBr	30	35
Au	AuCl ₃	16	33
Ni	NiCl ₂	3.1	4.7
Mixed Nanoporous Metal Systems			
AuCu	AuCl ₃ , CuCl ₂	24 (Au)	25 (Au)
CuCo	CuCl ₂ , CoCl ₂	5.7 (Cu)	8.2 (Cu)

a comparison of the metal nanocrystallite size (calculated via the Scherrer formula)³⁸ of each crystalline metal before and after methanol purification. The nanocrystals experience 20–100% growth, depending on the metal. In contrast, the metal XRD signatures for the Fe and Co samples are not affected by the purification process. For these, nanocomposite and purified metal XRD patterns display the same featureless signature that corresponds to the amorphous metal.

Iron, cobalt, and nickel are ferromagnetic metals, which allowed for magnetic measurements of their corresponding nanoporous structures (Figure 6). For the amorphous samples (nanoporous Fe and Co), magnetic measurements were used instead of XRD to analyze the metal network structure before and after purification. Coercivity and remanence of magnetic nanomaterials are strongly related to their particle (*i.e.*, magnetic domain) size and packing density.^{39–42} The sizes of Fe, Co, and Ni nanoparticles in LiCl matrix are estimated to be 3, 8, and 10 nm, respectively, according to the reported values of the coercivity of Co,⁴³ Fe,⁴⁴ and Ni⁴⁵ nanoparticles. It is noteworthy that the coercivity of Fe and Co samples decrease after the removal of LiCl (Figure 6a and b respectively). Kechrakos and Trohidou^{41,46} performed Monte Carlo simulation on a random assembly of ferromagnetic particles. They determined that coercivity and remanence decrease with increasing volume fraction of metal particle. In the Fe/LiCl and Co/LiCl nanocomposites, the dipolar interaction between metal nanoparticles is weaker than for a dense assembly of Fe and Co nanoparticles because they are separated by LiCl matrix. After the removal of LiCl with methanol, the metal nanoparticles agglomerate, and the dipolar interaction increases.⁴² The coercivity and remanence of pure Fe is very small because its pore size is only 2 nm, which causes strong dipolar interaction. The increase in coercivity and remanence of the pure Ni after the removal of LiCl (Figure 6c), which is opposite to the Fe and Co samples, happens because the magnetic dipole of Ni is smaller than Fe and Co. Ni nanoparticles only weakly interact with each other, suppressing the decrease in coercivity and remanence.⁴¹ In addition, the XRD pattern of Ni/LiCl and pure Ni shows increasing crystal size after the removal of LiCl (Table 2), which increases the blocking temperature of superparamagnetism.⁴⁷

Reconstruction during methanol purification causes a lower than theoretical cumulative pore volume for all samples. The metal structures with ligaments thicker than 20 nm (Cu, Au, Ni) all exhibit crystal growth as shown in the XRD studies. For these samples, the increase in nanocrystal size is consistent with a loss of pore volume, as the metals that showed larger crystal growth had a larger difference between theoretical and measured pore volume. The Fe and Co samples are particularly interesting because they have the highest specific surface area, yet their measured pore volume is lower than the Cu and Ni samples even though it is predicted to be higher. Recrystallization does not account for this because there is no evidence of crystal growth in XRD. Magnetic coercivity measurements also do not present evidence of magnetic domain growth, so there must be a separate type of reconstruction occurring.

One possibility is that because the Fe and Co metal networks are formed by exceptionally thin ligaments (<20 nm thick), they are not very robust, and removing the supporting lithium halide matrix causes the structure to partially collapse during purification. Thinner metal ligaments would then lead to a weaker structure and greater collapse, resulting in a larger difference between measured and theoretical pore volume. Data displayed in Table 1 of NPMs formed from CoCl₂, FeCl₂, and FeCl₃ support this trend, with nanoporous Fe via FeCl₃ exhibiting the thinnest ligaments and the largest discrepancy between measured and theoretical pore volume. SEM and TEM images in Figure 2 and Figure 3 show that space remains between the ligaments in these samples, confirming that the collapse is partial. Therefore, it retains high specific surface area despite the lower pore volume.

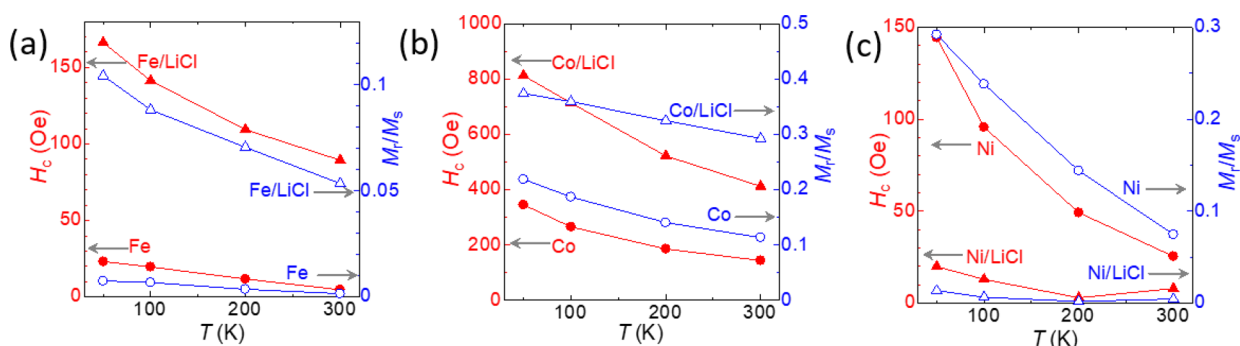


Figure 6. Coercivity (H_c) and remanence (M_r/M_s) of (a) Fe and Fe/LiCl, (b) Co and Co/LiCl, and (c) Ni and Ni/LiCl. H_c and M_r/M_s of Fe/LiCl and Co/LiCl decrease after removal of LiCl due to increased dipolar interaction between the metal nanoparticles. Conversely, those values for Ni/LiCl increase after removal of LiCl because of the weak dipolar interaction and crystal growth.

The reconstruction phenomena stem from the nature of the metal ligament network while it is still encased in the metal/lithium halide nanocomposite. During the conversion reaction, the metal and halide phases are thermodynamically driven to separate, but the more abundant lithium halide likely provides a kinetic barrier that prevents the metal atoms from coalescing over longer distances. Thus, while in the nanocomposite, the metal is locked in a metastable state by the lithium halide. Once the lithium halide is removed, that kinetic barrier is lowered, and reconstruction is favored to relax excess surface tension on the newly exposed metal surface.

Mixed Nanoporous Metals (MNPMS). We have also demonstrated that conversion synthesis can be used to fabricate MNPMS by converting coprecipitated precursors. Here, two metal halide precursors with the same anion but different transition-metal cations are mutually dissolved into methanol to form a homogeneous solution. The solution is then heated under vacuum to evaporate the solvent and coprecipitate the precursor compounds. These mixed precursors are reacted with *n*-BuLi to form metal/lithium halide nanocomposites and purified with methanol to generate MNPMS which have the familiar filament-network morphologies as the pure NPMs, but with filaments of two metals. Nanoporous gold-copper, cobalt-iron, and copper-cobalt mixtures were synthesized with this method.

Each of the three systems exhibited varied results. The Co-Fe system was the simplest: SEM and EDX images in Figure 7 and

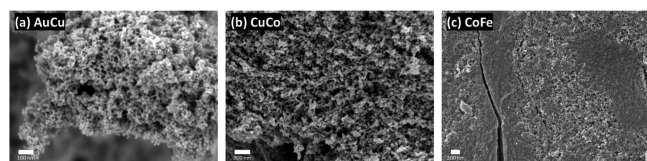


Figure 7. SEM images of MNPMS synthesized from coprecipitated chloride precursors. (a) Nanoporous AuCu, from coprecipitated $\text{AuCl}_3 + \text{CuCl}_2$. (b) Nanoporous CuCo, from coprecipitated $\text{CuCl}_2 + \text{CoCl}_2$. (c) Nanoporous CoFe, from coprecipitated CoCl_2 and FeCl_2 .

Figure S6 showed distinct, micron-sized regions of nanoporous Fe and Co. This is corroborated by BET data, which measured specific surface area and average pore width values to be averaged between that of pure nanoporous Fe and Co, as shown in Table 1. In contrast, the Au-Cu and Cu-Co systems showed improved mixing, which surprisingly resulted in nanoporous materials with surface area values that matched

or outperformed pure NPMs formed from the constituent precursors.

Nanoporous Au-Cu was originally synthesized from a coprecipitated methanol solution of 1:1 weight ratio of AuCl_3 and CuCl_2 , which corresponded to an approximate 3:2 weight ratio of Au to Cu in the final MNPMS. SEM images and EDX spectra shown in Figure 7 and Figure S3 indicate that the nanoporous structure consists of larger gold branches surrounded by much finer copper ligaments. The copper covers much of the surface, with the large underlying gold filaments occasionally visible. SEM images show the copper filaments are thinner in this MNPMS than in pure nanoporous copper from the same precursor. Thus, BET analysis measures a specific surface area very near that of nanoporous copper (approximately $15 \text{ m}^2/\text{g}$). This is despite that pure nanoporous gold has only 1/3 of the surface area as pure nanoporous copper and that gold is the weight-majority component in the mixture. A second Au-Cu MNPMS was synthesized with a 1:1 weight ratio between the metals to study the effect of adding additional Cu into the system. The resulting material measured an even greater specific surface area of $24.37 \text{ m}^2/\text{g}$, which is higher than either the pure Au or Cu NPM.

Nanoporous Cu-Co is an even more homogeneous metal network; SEM images and EDX (Figure 7 and Figure S5) show a consistent structure with both constituent metals appearing at approximately the same concentrations at the surface. However, this system exhibits surface properties that are far superior to either of the constituent pure NPMs. Shown in Table 1, the surface area of nanoporous Cu-Co was measured at $115.7 \text{ m}^2/\text{g}$, which is a 25% improvement over nanoporous Co and over $7.5\times$ greater than nanoporous Cu. The calculated pore width of 1.95 nm is also unexpectedly small and approaches that of nanoporous Fe from FeCl_3 precursor (1.8 nm pore width).

The nature of these mixed structures becomes apparent from X-ray analysis. XRD results in Figure 8 indicate that these mixed NPMs are nanoscopic mixtures of pure metal phases rather than a true, atomically mixed alloy. Then, Scherrer analysis of the broadened metal crystal peaks in the Au-Cu and Cu-Co diffraction patterns shows the structures are comprised of nanocrystallites (Table 2). This is similar to the nanoporous pure metals, but nanocrystallites in the mixed NPMs are estimated to be much smaller, particularly for Cu which shows 8 nm nanocrystallites in the Cu-Co system. Further, the mixed NPMs exhibit a much smaller difference in nanocrystal size before and after methanol purification, indicating that there is less crystal growth during the removal of LiCl, also displayed in Table 2. When comparing this crystal growth to that of the

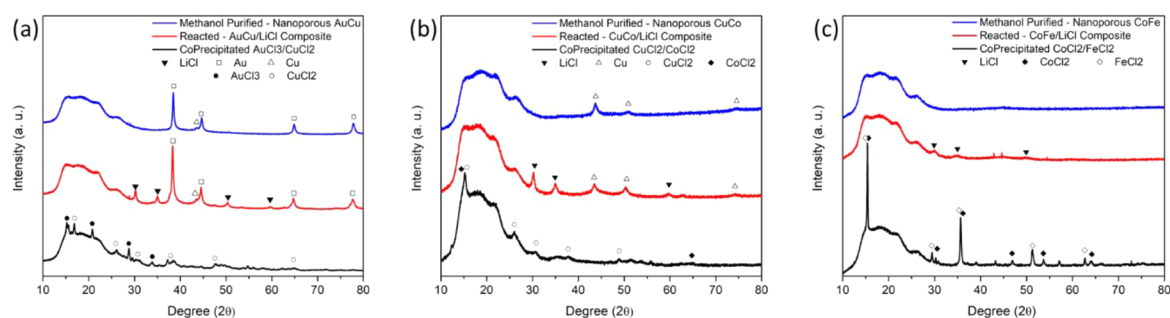


Figure 8. XRD patterns for MNPM samples, including patterns of the coprecipitated precursors, the metal/lithium halide nanocomposites, and the final mixed NPM products. (a) Nanoporous AuCu *via* AuCl₃ + CuCl₂. (b) Nanoporous CuCo *via* CuCl₂ + CoCl₂. (c) Nanoporous FeCo *via* FeCl₂ + CoCl₂.

pure metal samples, the effect in the MNPMs is greatly reduced.

The Au-Cu and Cu-Co MNPM systems have superior properties because their porous microstructures are more stable, both in their respective metal/lithium halide nanocomposite and NPM forms. In either system, the two constituent metals mutually stabilize one another. Nanostructured metals are typically unstable because interfacial interactions become dominant forces that drive grain growth and coarsening even at ambient temperatures.^{48,49} Alloying is a prominent technique used to stabilize nanocrystalline metals, where solute metal atoms can occupy grain boundary sites and relieve interfacial energy.⁵⁰ A similar effect likely occurs in MNPMs. For pure NPMs, the only interfaces remaining after the lithium halide is removed are those between nanocrystals of the pure metal. A percentage of these interfacial interactions are unfavorable, so recrystallization and grain growth occur. However, the presence of a second metal at such interfaces decreases the likelihood of excess migration and nanocrystal growth of the metal atoms during the conversion and methanol purification processes, resulting in smaller nanocrystallites in the nanocomposite for MNPMs. These smaller nanocrystallites equate to smaller nanoparticles of each constituent metal, which agglomerate together to construct a heterogeneous ligament network with improved specific surface area compared to the pure NPMs. This mechanism requires at least one of the constituent metals to be a relatively mobile element. Therefore, the Au-Cu and Cu-Co systems perform better than the Fe-Co system. Fe and Co are less mobile elements than Cu or Au. This allows them to form superior pure NPMs, but they are not mobile enough to form a thorough mixture of Co and Fe nanostructures as effectively as Au and Cu. Instead, they form isolated, micrometer-sized regions of pure NPM, resulting in properties that are averaged between that of pure nanoporous Fe and Co (Table 1).

CONCLUSION

In summary, with conversion reaction synthesis the nanoporous metal formation occurs in two phases. The nanoporous structure originally forms in the nanocomposites as the metal and lithium halide phases spinodally decompose as they are produced, with the metal atoms being thermodynamically driven together into a network of fine filaments surrounded by the corresponding lithium halide. The dimensions of the metal network are characteristic of the target metal atoms' mobility and the amount of lithium halide produced by the reaction between the precursor and the organolithium reagent. The lithium halide provides a kinetic barrier to excess metal atom

agglomeration, which locks the metal network into a metastable state. Then, removing the lithium with methanol reveals the porous network, but the purification process causes reconstruction that decreases the final pore volume.

Conversion synthesis of nanoporous metals is qualitatively similar to the dealloying method and can produce similar structures. If one uses each respective method to prepare nanoporous gold, both will produce similar ligamented networks with very similar specific surface area and pore volume.⁵¹ While the application of the dealloying method is determined by the availability of the alloy precursor and the removal of the reactive element, conversion synthesis is compatible with any metal halide precursor with an appropriate electrochemical potential, which allows us to synthesize pure nanoporous metal structures of a variety of transition metals. We are also able to synthesize mixed nanoporous metals from mixtures of precursors, which in some cases exhibit finer nanostructures and superior surface properties when compared to nanoporous structures of the constituent metals. Mixing precursors opens a large parameter space for further design and engineering of nanoporous metals and further proves the versatility of this synthesis method. With the abundance of compatible precursor candidates and with the simplicity and scalability of these methods, conversion synthesis provides a wide and accessible design space for the development of nanoporous metal technology.

METHODS

In a typical synthesis of a NPM, an anhydrous metal chloride (CoCl₂, CuCl₂, FeCl₃, *etc.*) is first dispersed in hexane at 10 mL per gram of precursor. Then, 1.6 M *n*-butyllithium solution in hexane is added at 1.25× stoichiometric ratio to guarantee complete consumption of the precursor. The reaction starts instantaneously, and the brightly colored chloride precursors turn black as they are converted into the metal/lithium halide nanocomposites. The solution is allowed to react undisturbed for 24 h. The solids are then isolated with filtration and rinsed with copious amounts of additional hexane. The resulting powder is air-dried.

To purify the composite and form a NPM, the nanocomposite powder is added to a 50 mL size fritted filter funnel, and 30 mL of anhydrous methanol is added and allowed to drain into a collection flask. This process is repeated once. The resulting powder is left to air-dry before collection and storage. This entire process is performed in an argon glovebox (<5 ppm of O₂ content), as the inert atmosphere is required to prevent the nanostructured metals from oxidizing.

Mixed metal chloride precursors are used to synthesize mixed NPMs. In a typical synthesis of the precursor, 1.0 g of each chloride precursor is fully dissolved into 20 mL of anhydrous methanol, forming a homogeneous solution. The solution is then rapidly evaporated under vacuum at 150 °C so the precursors mutually

coprecipitate. The mixed precursors are kept under vacuum and at 150 °C for at least 4 h after all the solvent has evaporated to ensure they are completely dry and no residual solvents remain. Once dry, the mixed precursors are converted and purified in the same manner as the pure precursors to produce MNPMs.

A rotating target powder diffractometer (Bruker D2-Phaser) using Cu K α radiation ($\lambda = 1.5406 \text{ \AA}$, 30 kV, 10 mA) was used for XRD studies of the nanocomposites and the purified metals in a 2θ range from 10 to 80° with scanning rate 0.02°/s and step size 0.05°. Kapton tape was secured over the powders on the circular sample targets in an Ar glovebox to avoid oxidation during data acquisition. For samples that exhibited well-defined XRD patterns, diffraction peaks were indexed using data from the Inorganic Crystal Structure Database (ICSD),⁴⁵ and nanocrystallite size was estimated from the half-maximum width and 2θ positions of the broadened diffraction peaks according to the Scherrer formula.³³

N₂ gas sorption analysis was performed with a Quantachrome Autosorb-iQ/MPXR surface area and porosity analyzer. Each sample was loaded into the quartz sample tube in an Ar glovebox and sealed with parafilm so each sample could be transported to the analyzer without exposure to ambient oxygen. Once inserted into the machine, each sample was degassed under vacuum at 80 °C for 8 h. The N₂ adsorption–desorption isotherms were then obtained with the analyzer at liquid nitrogen temperature (78 K). Average pore width and cumulative pore volume was calculated from the recorded isotherms using the NLDFT equilibrium model within the Quantachrome3 ASiQwin Software.⁴⁶

The SEM images were acquired with a Zeiss Sigma 500 microscope at 2.0 keV EHT voltage, and TEM images were obtained at 200 kV acceleration voltage on an FEI Tecnai-Sphera system. For SEM characterization, samples were mounted on a stage using double-sided carbon tape. For TEM characterization, a small amount powder sample was dispersed in hexane and sonicated in an ultrasonic bath for 30 min. A drop of the dispersed sample was placed onto a copper-coated TEM grid and dried inside an Ar glovebox. For both SEM and TEM, the prepared samples were sealed in an aluminum lined bag within an Ar glovebox so they could be transported to the microscope without exposure to ambient air. The resulting images of the NPMs in conjunction with ImageJ software were used to estimate the approximate ligament thickness of each sample.⁵²

Coercivity and remanence of Fe, Co, and Ni samples and their composite with LiCl were measured by vibrating sample magnetometer (VSM, VersaLab, Quantum Design, USA) at 50–300 K. In the Ar filled glovebox (O₂ < 5 ppm), the powder samples were weighed and dispersed on a 4 × 4 mm² plastic plate and sealed with Kapton tape to prevent oxidation. The magnetic moment of pure LiCl was negligibly small compared to the value of Fe, Co, and Ni samples.

ASSOCIATED CONTENT

Supporting Information

The Supporting Information is available free of charge on the ACS Publications website at DOI: 10.1021/acsnano.7b06667.

Additional experimental details for materials synthesis and characterization data (PDF)

AUTHOR INFORMATION

Corresponding Author

*E-mail: piliu@eng.ucsd.edu.

ORCID

Ping Liu: 0000-0002-1488-1668

Notes

The authors declare no competing financial interest.

ACKNOWLEDGMENTS

This work was supported by faculty start-up funding from the University of California, San Diego (UCSD). The authors

thank F. Ji and Z. Chen for BET consultation and measurements as well as H. Ren and E. Fullerton for providing magnetic measurements. This work was performed in part at the San Diego Nanotechnology Infrastructure (SDNI) of UCSD, a member of the National Nanotechnology Coordinated Infrastructure, which is supported by the National Science Foundation (grant ECCS-1542148). We thank J. Bouwer and T. S. Baker of the Cryo-Electron Microscopy Facility, UCSD Department of Chemistry for guidance with TEM experiments.

REFERENCES

- (1) Ding, Y.; Kim, Y. J.; Erlebacher, J. Nanoporous Gold Leaf: “Ancient Technology.” *Adv. Mater.* **2004**, *16*, 1897–1900.
- (2) Ding, Y.; Chen, M. Nanoporous Metals for Catalytic and Optical Applications. *MRS Bull.* **2009**, *34*, S69–S76.
- (3) Dixon, M. C.; Daniel, T. A.; Hieda, M.; Smilgies, D. M.; Chan, M. H. W.; Allara, D. L. Preparation, Structure, and Optical Properties of Nanoporous Gold Thin Films. *Langmuir* **2007**, *23*, 2414–2422.
- (4) Yu, F.; Ahl, S.; Caminade, A.-M.; Majoral, J.-P.; Knoll, W.; Erlebacher, J. Simultaneous Excitation of Propagating and Localized Surface Plasmon Resonance in Nanoporous Gold Membranes. *Anal. Chem.* **2006**, *78*, 7346–7350.
- (5) Lang, X.; Hirata, A.; Fujita, T.; Chen, M. Nanoporous Metal/Oxide Hybrid Electrodes for Electrochemical Supercapacitors. *Nat. Nanotechnol.* **2011**, *6*, 232.
- (6) Guo, X.; Han, J.; Liu, P.; Chen, L.; Ito, Y.; Jian, Z.; Jin, T.; Hirata, A.; Li, F.; Fujita, T.; Asao, N.; Zhou, H.; Chen, M. Hierarchical Nanoporosity Enhanced Reversible Capacity of Bicontinuous Nanoporous Metal Based Li-O₂ Battery. *Sci. Rep.* **2016**, *6*, 33466.
- (7) Jin, H. J.; Weissmüller, J. Bulk Nanoporous Metal for Actuation. *Adv. Eng. Mater.* **2010**, *12*, 714–723.
- (8) Yi Ding, Y. Z. Nanoporous Metals. In *Handbook of Nanomaterials*; Vajtai, R., Ed.; Springer: Berlin, 2013; pp 779–811.
- (9) Tappan, B. C.; Steiner, S. A.; Luther, E. P. Nanoporous Metal Foams. *Angew. Chem., Int. Ed.* **2010**, *49*, 4544–4565.
- (10) McCue, I.; Benn, E.; Gaskey, B.; Erlebacher, J. Dealloying and Dealloyed Materials. *Annu. Rev. Mater. Res.* **2016**, *46*, 263–286.
- (11) Zhang, Z.; Wang, Y.; Qi, Z.; Zhang, W.; Qin, J.; Frenzel, J. Generalized Fabrication of Nanoporous Metals (Au, Pd, Pt, Ag, and Cu) Through Chemical Dealloying. *J. Phys. Chem. C* **2009**, *113*, 12629–12636.
- (12) Erlebacher, J.; Aziz, M. J.; Karma, A.; Dimitrov, N.; Sieradzki, K. Evolution of Nanoporosity in Dealloying. *Nature* **2001**, *410*, 450–453.
- (13) Bai, Q.; Wang, Y.; Zhang, J.; Ding, Y.; Peng, Z.; Zhang, Z. Hierarchically Nanoporous Nickel-Based Actuators with Giant Reversible Strain and Ultrahigh Work Density. *J. Mater. Chem. C* **2016**, *4*, 45–52.
- (14) Hsueh, H. Y.; Huang, Y. C.; Ho, R. M.; Lai, C. H.; Makida, T.; Hasegawa, H. Nanoporous Gyroid Nickel from Block Copolymer Templates via Electroless Plating. *Adv. Mater.* **2011**, *23*, 3041–3046.
- (15) Tang, S.; Vongehr, S.; Wang, Y.; Cui, J.; Wang, X.; Meng, X. Versatile Synthesis of High Surface Area Multi-Metallic Nanosponges Allowing Control Over Nanostructure and Alloying for Catalysis and SERS Detection. *J. Mater. Chem. A* **2014**, *2*, 3648–3660.
- (16) Krishna, K. S.; Sandeep, C. S.; Philip, R.; Eswaramoorthy, M. Mixing does the Magic: a Rapid Synthesis of High Surface Area Noble Metal Nanosponges Showing Broadband Nonlinear Optical Response. *ACS Nano* **2010**, *4*, 2681–2688.
- (17) Naguib, M.; Kurtoglu, M.; Presser, V.; Lu, J.; Niu, J.; Heon, M.; Hultman, L.; Gogotsi, Y.; Barsoum, M. W. Two-Dimensional Nanocrystals Produced by Exfoliation of Ti₃AlC₂. *Adv. Mater.* **2011**, *23*, 4248–4253.
- (18) Naguib, M.; Mochalin, V. N.; Barsoum, M. W.; Gogotsi, Y. 25th Anniversary Article: MXenes: A New Family of Two-Dimensional Materials. *Adv. Mater.* **2014**, *26*, 992–1005.

- (19) Zhang, J.; Li, C. M. Nanoporous Metals: Fabrication Strategies and Advanced Electrochemical Applications in Catalysis, Sensing and Energy Systems. *Chem. Soc. Rev.* **2012**, *41*, 7016–7031.
- (20) Xu, C.; Liu, Y.; Wang, J.; Geng, H.; Qiu, H. Nanoporous PdCu Alloy for Formic Acid Electro-Oxidation. *J. Power Sources* **2012**, *199*, 124–131.
- (21) Malini, R.; Uma, U.; Sheela, T.; Ganesan, M.; Renganathan, N. Conversion Reactions: a New Pathway to Realise Energy in Lithium-Ion Battery. *Ionics* **2009**, *15*, 301–307.
- (22) Amatucci, G. G.; Pereira, N. Fluoride Based Electrode Materials for Advanced Energy Storage Devices. *J. Fluorine Chem.* **2007**, *128*, 243–262.
- (23) Badway, F.; Pereira, N.; Cosandey, F.; Amatucci, G. G. Carbon-Metal Fluoride Nanocomposites: Structure and Electrochemistry of FeF₃. *C. J. Electrochem. Soc.* **2003**, *150*, A1209–A1218.
- (24) Wang, F.; Robert, R.; Chernova, N. A.; Pereira, N.; Omenya, F.; Badway, F.; Hua, X.; Ruotolo, M.; Zhang, R.; Wu, L.; Volkov, V.; Su, D.; Key, B.; Whittingham, M. S.; Grey, C. P.; Amatucci, G. G.; Zhu, Y.; Graetz, J. Conversion Reaction Mechanisms in Lithium Ion Batteries: Study of the Binary Metal Fluoride Electrodes. *J. Am. Chem. Soc.* **2011**, *133*, 18828–18836.
- (25) Chang, Y.-H.; Chiu, C. W.; Chen, Y. C.; Wu, C. C.; Tsai, C. P.; Wang, J. L.; Chiu, H. T. Syntheses of Nano-Sized Cubic Phase Early Transition Metal Carbides from Metal Chlorides and n-Butyllithium. *J. Mater. Chem.* **2002**, *12*, 2189–2191.
- (26) Suslick, K. S.; Choe, S. B.; Cichowlas, A. A.; Grinstaff, M. W. Sonochemical Synthesis of Amorphous Iron. *Nature* **1991**, *353*, 414–416.
- (27) Wang, Z.; Zuo, Y.; Yao, Y.; Xi, L.; Du, J.; Wang, J.; Xue, D. Microwave Absorption Properties of Amorphous Iron Nanostructures Fabricated by a High-Yield Method. *J. Phys. D: Appl. Phys.* **2013**, *46*, 135002.
- (28) Khalfaoui, M.; Knani, S.; Hachicha, M. A.; Lamine, A. B. New Theoretical Expressions for the Five Adsorption Type Isotherms Classified by BET Based on Statistical Physics Treatment. *J. Colloid Interface Sci.* **2003**, *263*, 350–356.
- (29) Sing, K. S. W.; Williams, R. T. Physisorption Hysteresis Loops and the Characterization of Nanoporous Materials. *Adsorpt. Sci. Technol.* **2004**, *22*, 773–782.
- (30) Seaton, N. A. Determination of the Connectivity of Porous Solids from Nitrogen Sorption Measurements. *Chem. Eng. Sci.* **1991**, *46*, 1895–1909.
- (31) Cheng, J. P.; Chen, X.; Wu, J.-S.; Liu, F.; Zhang, X. B.; Dravid, V. P. Porous Cobalt Oxides with Tunable Hierarchical Morphologies for Supercapacitor Electrodes. *CrystEngComm* **2012**, *14*, 6702–6709.
- (32) Yang, P.; Zhao, D.; Margolese, D. I.; Chmelka, B. F.; Stucky, G. D. Generalized Syntheses of Large-Pore Mesoporous Metal Oxides with Semicrystalline Frameworks. *Nature* **1998**, *396*, 152–155.
- (33) Golden, J. H.; DiSalvo, F. J.; Frechet, J. M. Room-Temperature Synthesis of (LiMo₃Se₃)_n and the Determination of the Relative Reduction Potential of tert-Butyllithium. *Chem. Mater.* **1994**, *6*, 844–849.
- (34) Wang, F.; Yu, H.-C.; Chen, M.-H.; Wu, L.; Pereira, N.; Thornton, K.; Van der Ven, A.; Zhu, Y.; Amatucci, G. G.; Graetz, J. Tracking Lithium Transport and Electrochemical Reactions in Nanoparticles. *Nat. Commun.* **2012**, *3*, 1201.
- (35) Miyamoto, M.; Takeda, H. Atomic Diffusion Coefficients Calculated for Transition Metals in Olivine. *Nature* **1983**, *303*, 602–603.
- (36) Naghavi, S. S.; Hegde, V. I.; Wolverton, C. Diffusion Coefficients of Transition Metals in fcc Cobalt. *Acta Mater.* **2017**, *132*, 467–478.
- (37) Weber, E. R. Transition Metals in Silicon. *Appl. Phys. A: Solids Surf.* **1983**, *30*, 1–22.
- (38) Patterson, A. L. The Scherrer Formula for X-Ray Particle Size Determination. *Phys. Rev.* **1939**, *56*, 978–982.
- (39) Herzer, G. Grain Size Dependence of Coercivity and Permeability in Nanocrystalline Ferromagnets. *IEEE Trans. Magn.* **1990**, *26*, 1397–1402.
- (40) Gong, W.; Li, H.; Zhao, Z.; Chen, J. Ultrafine Particles of Fe, Co, and Ni Ferromagnetic Metals. *J. Appl. Phys.* **1991**, *69*, 5119–5121.
- (41) Kechrakos, D.; Trohidou, K. Magnetic Properties of Dipolar Interacting Single-Domain Particles. *Phys. Rev. B: Condens. Matter Mater. Phys.* **1998**, *58*, 12169.
- (42) Chantrell, R.; Walmsley, N.; Gore, J.; Maylin, M. Calculations of the Susceptibility of Interacting Superparamagnetic Particles. *Phys. Rev. B: Condens. Matter Mater. Phys.* **2000**, *63*, 024410.
- (43) Gangopadhyay, S.; Hadjipanayis, G.; Sorensen, C.; Klabunde, K. Magnetic Properties of Ultrafine Co Particles. *IEEE Trans. Magn.* **1992**, *28*, 3174–3176.
- (44) Gangopadhyay, S.; Hadjipanayis, G.; Dale, B.; Sorensen, C.; Klabunde, K.; Papaefthymiou, V.; Kostikas, A. Magnetic Properties of Ultrafine Iron Particles. *Phys. Rev. B: Condens. Matter Mater. Phys.* **1992**, *45*, 9778.
- (45) Du, Y. W.; Xu, M. X.; Wu, J.; Shi, Y. B.; Lu, H. X.; Xue, R. H. Magnetic Properties of Ultrafine Nickel Particles. *J. Appl. Phys.* **1991**, *70*, 5903–5905.
- (46) Kechrakos, D.; Trohidou, K. Effects of Dipolar Interactions on the Magnetic Properties of Granular Solids. *J. Magn. Magn. Mater.* **1998**, *177*, 943–944.
- (47) Majetich, S.; Sachan, M. Magnetostatic Interactions in Magnetic Nanoparticle Assemblies: Energy, Time and Length Scales. *J. Phys. D: Appl. Phys.* **2006**, *39*, R407.
- (48) Ames, M.; Markmann, J.; Karos, R.; Michels, A.; Tschöpe, A.; Birringer, R. Unraveling the Nature of Room Temperature Grain Growth in Nanocrystalline Materials. *Acta Mater.* **2008**, *56*, 4255–4266.
- (49) Weertman, J. R.; Farkas, D.; Hemker, K.; Kung, H.; Mayo, M.; Mitra, R.; Swygenhoven, H. V. Structure and Mechanical Behavior of Bulk Nanocrystalline Materials. *MRS Bull.* **1999**, *24*, 44–53.
- (50) Chookajorn, T.; Murdoch, H. A.; Schuh, C. A. Design of Stable Nanocrystalline Alloys. *Science* **2012**, *337*, 951.
- (51) Tan, Y. H.; Davis, J. A.; Fujikawa, K.; Ganesh, N. V.; Demchenko, A. V.; Stine, K. J. Surface Area and Pore Size Characteristics of Nanoporous Gold Subjected to Thermal, Mechanical, or Surface Modification Studied Using Gas Adsorption Isotherms, Cyclic Voltammetry, Thermogravimetric Analysis, and Scanning Electron Microscopy. *J. Mater. Chem.* **2012**, *22*, 6733–6745.
- (52) Abramoff, M. D.; Magalhaes, P. J.; Ram, S. J. Image Processing with ImageJ. *Biophotonics Int.* **2004**, *11*, 36–42.